Role of Sn in the Regeneration of Pt/γ-Al₂O₃ Light Alkane Dehydrogenation Catalysts

Hien N. Pham,[†] Jesper J. H. B. Sattler,[‡] Bert M. Weckhuysen,*,[‡] and Abhaya K. Datye*,[†]

[†]Department of Chemical & Biological Engineering and Center for Microengineered Materials, University of New Mexico, Albuquerque, New Mexico 87131, United States

[‡]Inorganic Chemistry and Catalysis Group, Debye Institute for Nanomaterials Science, Utrecht University, Universiteitsweg 99, 3584 CG Utrecht, The Netherlands

Ⓢ *Supporting Information*

ABSTRACT: Alumina-supported Pt is one of the major industrial catalysts for light alkane dehydrogenation. This catalyst loses activity during reaction, with coke formation often considered as the reason for deactivation. As we show in this study, the amount and nature of carbon deposits do not directly correlate with the loss of activity. Rather, it is the transformation of subnanometer Pt species into larger Pt nanoparticles that appears to be responsible for the loss of catalytic activity. Surprisingly, a portion of the Sn remains atomically dispersed on the alumina surface in the spent catalyst and helps in the redispersion of the Pt. In the absence of Sn on the alumina support, the larger Pt nanoparticles formed during reaction are not redispersed during oxidative regeneration. It is known that Sn is added as a promoter in the industrial catalyst to help in achieving high propene selectivity and to minimize coke formation. This work shows that an important role of Sn is to help in the regeneration of Pt, by providing nucleation sites on the alumina surface. Aberration-corrected scanning transmission electron microscopy helps to provide unique insights into the operating characteristics of an industrially important catalyst by demonstrating the role of promoter elements, such as Sn, in the oxidative regeneration of Pt on γ-Al₂O₃.

KEYWORDS: Pt/γ-Al₂O₃, Pt-Sn/γ-Al₂O₃, oxidative regeneration, nucleation sites, propane dehydrogenation, sintering, coking, STEM/HRTEM
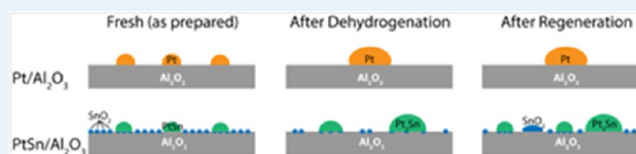
1. INTRODUCTION

There is an ever-increasing demand for light alkenes, including propene, because propene is a very important chemical intermediate used for the production of a wide variety of bulk chemicals and materials, including polymers.[1,2] The primary route for the manufacture of propene is the selective dehydrogenation of propane,[3−10] a paraffin that can be obtained from low-cost feedstocks, such as shale gas deposits, which are now becoming available.[11,12] Propane dehydrogenation (PDH) occurs at high temperatures using supported CrO$_x$[13−15] or Pt catalysts. The drawback to light paraffin dehydrogenation processes is coking, which deactivates the catalyst and reduces the selectivity toward olefins. Sintering of the metal phase under high-temperature conditions is another very important factor for deactivation of the catalysts, and extensive studies have been conducted to determine factors that can stabilize and inhibit sintering of the metal phase. For example, in an alumina-supported Pt catalyst treated under high-temperature oxidizing conditions, scanning transmission electron microscopy/transmission electron microscopy (STEM/TEM) imaging,[27] Al magic angle spinning (MAS) nuclear magnetic resonance (NMR), extended X-ray absorption fine structure (EXAFS), and density functional theory (DFT) calculations were used to show that atomic or subnanometer Pt species could be stabilized and become sinter resistant because of their strong interactions with the pentacoordinated Al³⁺ sites

on the γ-Al₂O₃(100) surface.[16,17] Typically, a second metal component, such as Sn[14,18−24] and Ga,[2,25−28] is added to the catalyst formulation, which forms an alloy with Pt under reaction conditions, increasing conversion and propene selectivity, inhibiting metal sintering, and suppressing coke formation. Recently, more earth abundant metals, such as Cu, have been used as promoters to form an alloy with Pt with similar effects, such as inhibiting propene adsorption and suppressing side reactions, increasing propene selectivity and yield, and reducing the level of coke formation.[29] To remove the coke, catalysts are regenerated under oxidizing (or oxychlorination) conditions followed by H₂ reduction to reactivate the catalysts. Such continuous treatments, however, may not fully restore catalytic performance, leading to eventual loss of activity and selectivity in consecutive cycles.[19,30] Therefore, a better understanding of the deactivation and regeneration processes is essential for the design of improved light alkane dehydrogenation catalysts.

Alumina-supported Pt−Sn catalysts have been extensively used for light alkane dehydrogenation;[14,19−24] recently, they have been used for jet fuel and hydrocarbon blend partial dehydrogenation.[31−35] The addition of Sn as a promoter helps

to modify both the Pt active phase and the support. Because the Pt−alkene interaction is stronger than the Pt−alkane interaction, undesired side reactions such as hydrogenolysis and isomerization can occur; Sn weakens the Pt−alkene interaction without weakening the Pt−alkane interaction and, therefore, suppresses the side reactions.[14] This is how Sn is thought to influence the selectivity of the catalyst. The Sn also helps to minimize sintering of the Pt metal phase, inhibit the acidity of the support, and facilitate the diffusion of coke species from Pt to the support. Aside from the beneficial properties of the Sn promoter, there is an ongoing debate about the electronic[36,37] and geometric[38] effects of adding Sn to Pt in order to explain the reaction mechanism through which Sn influences the catalytic performance of light alkane dehydrogenation.

In this work, we describe another important role of Sn in these catalysts. We found that the initial activity of Pt-Sn/γ-Al$_2$O$_3$ could be regenerated over multiple cycles after this catalyst had been deactivated during PDH. Such regeneration was only possible after the first cycle for Pt/γ-Al$_2$O$_3$, with the catalyst progressively losing its activity in subsequent cycles as larger Pt nanoparticles were formed. We conclude that a critical difference between the monometallic and bimetallic Pt-based alkane dehydrogenation catalysts is in the regeneration step, wherein Sn provides nucleation sites to redisperse Pt and/or re-form subnanometer Pt clusters in the Pt−Sn catalyst. The coke content of the catalyst material in each cycle was examined to see if the loss of activity was related to the amount of carbon deposited. The results show that the extent of deactivation of Pt/γ-Al$_2$O$_3$ and Pt-Sn/γ-Al$_2$O$_3$ could not be correlated with coke deposits, as is commonly assumed in the literature.[22,24,30,39,40] This is because the coke can be effectively transported to the support, as suggested previously,[19,29,41,42] allowing the active sites to continue functioning.

2. EXPERIMENTAL SECTION

2.1. Catalyst Preparation. Two catalyst materials, 0.5 wt % Pt/γ-Al$_2$O$_3$ and 0.5 wt % Pt−1.5 wt % Sn/γ-Al$_2$O$_3$, were prepared by incipient wetness impregnation of a solution containing H$_2$PtCl$_6$(H$_2$O)$_x$ (38 wt % Pt, Sigma-Aldrich) with or without SnCl$_2$(H$_2$O)$_2$ (98%, VWR Int.) onto a puralox alumina support (SASOL, γ-Al$_2$O$_3$). The catalysts were dried for 2 h at 60 °C and overnight at 120 °C, followed by calcination at 560 °C for 3 h.

2.2. Catalyst Characterization. The catalysts were dispersed in ethanol and mounted on holey carbon grids for examination in high-angle annular dark field (HAADF) mode using two electron microscopes. One was a JEOL 2010F 200 kV transmission electron microscope (resolution of 0.14 nm) equipped with an Oxford Energy dispersive spectroscopy system for elemental analysis. The other was a JEOL JEM ARMS200CF 200 kV aberration-corrected (AC) transmission electron microscope (resolution of 0.08 nm) also equipped with an Oxford Energy dispersive spectroscopy system but with a wide area detector for atomic-resolution elemental analysis. The AC microscope was used to determine if single atoms were present in the spent catalysts. For each sample, several STEM images were used to count Pt or PtSn particle sizes, with 10−60 particles measured per image. The particle size distribution was presented in a histogram, and the mean and standard deviation were calculated from the total number of particles counted (∼700−800) in each sample. To analyze the carbon deposits in the spent catalysts after the 1st and 10th PDH cycles,

thermogravimetric analysis (TGA) measurements were performed using a PerkinElmer 1 Analyzer. The catalyst (10−25 mg) was dried under Ar at 150 °C and then heated in O$_2$ from room temperature to 900 °C (rate of 10 °C min^{-1}). Operando Raman spectroscopy has been described elsewhere.[43]

2.3. Catalyst Testing. A tubular quartz reactor was filled with 0.3 g of catalyst and placed inside an oven. The catalyst was pretreated under H$_2$ at 600 °C for 1 h to obtain the catalytically active metallic Pt phase, after which pure propane at a rate of 9 mL min^{-1} flowed through the catalyst bed (WHSV = 3.2 h^{-1}) and dehydrogenation reaction was performed for 6 h. After the reaction (1st cycle), the deactivated catalyst was regenerated by passing a mixture of O$_2$ and He over the catalyst at 600 °C for 1 h followed by a 45 min H$_2$ reduction step, and the next PDH reaction was performed for 6 h (2nd cycle) for a total of 10 dehydrogenation−regeneration cycles. The products were collected at 5 min intervals using a gas chromatograph (GC) equipped with FID (Porabond-Q column) and TCD (Carboxan column) detectors.

3. RESULTS

Catalytic testing of the Pt/γ-Al$_2$O$_3$ and Pt-Sn/γ-Al$_2$O$_3$ catalysts during prolonged PDH reactions (at 600 °C and 1 bar) consisted of 10 dehydrogenation−regeneration cycles. Propane conversion and selectivity toward propene are shown in Figure 1, with the data at different periods of time during the cycles
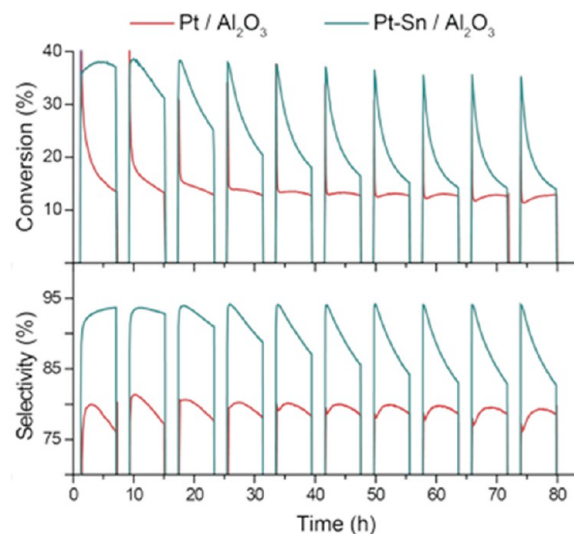

Figure 1. Propane dehydrogenation (PDH) activity at 600 °C using Pt/γ-Al$_2$O$_3$ and Pt-Sn/γ-Al$_2$O$_3$. After each PDH cycle, the catalyst materials were regenerated by flowing O$_2$/He at 600 °C followed by H$_2$ reduction at 600 °C, for a total of 10 dehydrogenation−regeneration cycles.

summarized in Table 1. Both catalyst materials initially show similar high propane conversions (35.0 vs 35.6%); however, Pt/γ-Al$_2$O$_3$ deactivates rapidly, whereas the conversion remains high and stable for Pt-Sn/γ-Al$_2$O$_3$ during the first PDH cycle. After the third cycle, the Pt catalyst displays the lowest propane conversion (i.e., 17.1%). The Pt-Sn/γ-Al$_2$O$_3$ catalyst shows significant deactivation beginning with the second cycle, with an increasing level of deactivation through the fifth cycle, after which there is a similar activity profile in the subsequent cycles. At the end of the 10th cycle, propane conversion for Pt-Sn/γ-

Table 1. Propane Conversion (X) and Propene Selectivity (S) of the Two Pt-Based Catalyst Materials under Study at Different Periods of Time during the 10 Successive Dehydrogenation–Regeneration Cycles

cycle	Pt/γ-Al$_2$O$_3$		Pt-Sn/γ-Al$_2$O$_3$	
	X (%)	S (%)	X (%)	S (%)
start of cycle 1	35.0	72.1	35.6	88.5
end of cycle 1	13.5	76.0	37.2	93.7
start of cycle 3	17.1	80.6	38.2	92.9
end of cycle 3	12.9	77.7	25.2	91.1
start of cycle 10	13.9	77.2	35.4	94.0
end of cycle 10	12.9	78.6	14.1	82.8

Al$_2$O$_3$ (14.1%) is similar to the conversion for Pt/γ-Al$_2$O$_3$ (12.9%), but the major difference is the ease with which the reactivity of the Sn-containing catalyst is restored after each regeneration step. Sn also plays a significant role in influencing the selectivity, with Pt-Sn/γ-Al$_2$O$_3$ showing selectivity toward propene (88.5%) significantly higher than that of Pt/γ-Al$_2$O$_3$ even in its fresh state (72.1%).

TGA was used to quantify the amount of coke present on the spent catalysts by combusting the carbon deposits under flowing O$_2$, and the resultant loss of weight was measured as a function of temperature. The amount of coke present on the spent catalysts after 1 and 10 PDH cycles is summarized in Table 2, and the plot of the weight loss of carbon as a function

Table 2. Weight Losses of Carbon and Combustion Temperatures of the Pt-Based Catalyst Materials under Study after the 1st and 10th PDH Cycles

catalyst sample	weight loss (wt %)		$T_{combustion}$ (°C)	
	1st cycle	10th cycle	1st cycle	10th cycle
Pt/γ-Al$_2$O$_3$	6.2	6.4	440	480
Pt-Sn/γ-Al$_2$O$_3$	10.5	5.0	505	470

of temperature is shown in Figure 2. After the first cycle, coke combustion occurs at a much lower temperature for Pt/γ-Al$_2$O$_3$ than for Pt-Sn/γ-Al$_2$O$_3$, suggesting that carbon deposits are in the proximity of the Pt sites in the Pt catalyst, whereas for the Pt-Sn catalyst, carbon deposits are likely located on the alumina support because combustion occurs at a higher temperature.[22] After the 10th cycle, coke combustion temperatures have

changed for both catalysts, and the combustion profiles are now similar. In a previous study of olefin metathesis catalysts, we demonstrated by EFTEM how the coke can be present on the alumina support and not block the active sites.[44]

At the end of the first reaction cycle, more coke is deposited on Pt-Sn/γ-Al$_2$O$_3$ (10.5 wt %) than on Pt/γ-Al$_2$O$_3$ (6.2 wt %), but after the 10th cycle, less coke is deposited on Pt-Sn/γ-Al$_2$O$_3$ (5 wt %); there is no real change in the amount of coke deposited on Pt/γ-Al$_2$O$_3$ (6.4 wt %). Via examination of the dehydrogenation–regeneration cycles as shown in Figure 1 and the amount of carbon deposits as summarized in Table 2, there is no obvious correlation between the amount of coke on the spent catalysts and the final catalytic activity. After the first cycle, Pt-Sn/γ-Al$_2$O$_3$ has almost twice the amount of carbon as in Pt/γ-Al$_2$O$_3$, but Pt-Sn/γ-Al$_2$O$_3$ does not deactivate while Pt/γ-Al$_2$O$_3$ deactivates rapidly. After the 10th cycle, both samples show similar amounts of carbon, but Pt/γ-Al$_2$O$_3$ has been significantly deactivated compared to Pt-Sn/γ-Al$_2$O$_3$. This suggests that deactivation for all dehydrogenation–regeneration cycles is not due to blocking of the metal active sites by coke. Operando Raman spectra (Figure S1) are similar for all cycles (1st, 3rd, and 10th) in the spent Pt/γ-Al$_2$O$_3$ and Pt-Sn/γ-Al$_2$O$_3$ samples (D_1/G ratio $\sim$ 0.72), indicating a similar nature of carbon deposits in both samples. HRTEM of the spent Pt-Sn/γ-Al$_2$O$_3$ catalyst after the 10th cycle, as shown in Figure 3, does not show any carbon deposits on the metal surfaces, only on the surface of alumina. Previously, we demonstrated that 10 wt % carbon, forming close to a monolayer on the silica support, could be imaged via HRTEM.[45] We see a very similar morphology in deactivated Pt-Sn/γ-Al$_2$O$_3$ containing 5 wt % carbon, which is close to a monolayer (Figure 3). The HRTEM image shows a wormy surface layer on the spent catalyst, corresponding to the 3.4 Å interlayer spacing of graphite, which is absent after the catalyst has been treated under oxidizing conditions. We therefore conclude that the coke in this sample is located on the alumina support and does not block active sites, and therefore, deactivation may not be correlated with the amount and nature of coke deposits.[26] The results are also in agreement with the work of Sokolov et al.,[30] in which they found that the VO$_x$/MCM-41 catalyst showed the highest carbon deposit after four oxidative regeneration cycles with Pt-Sn/γ-Al$_2$O$_3$ showing the smallest carbon deposit, yet VO$_x$/MCM-41 was the most active and stable catalyst for PDH.
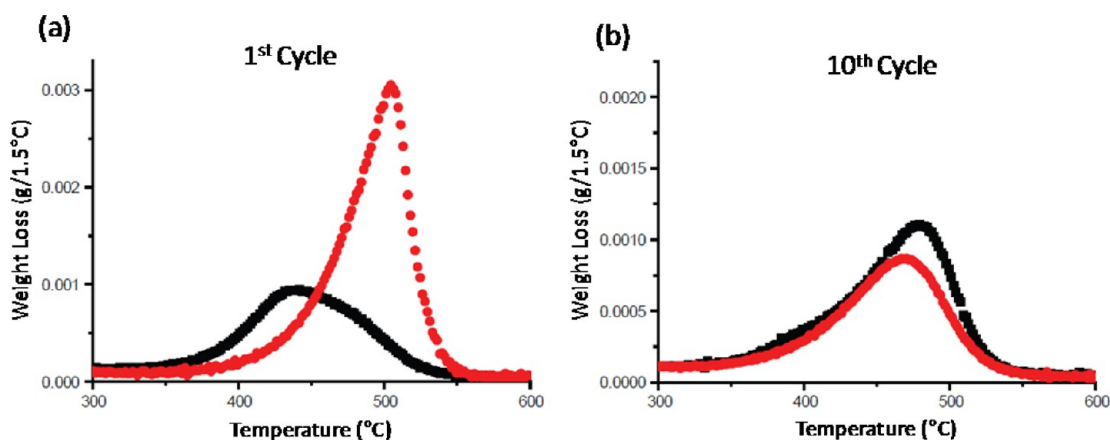

Figure 2. Derivative of the weight loss of carbon as a function of temperature for the Pt/γ-Al$_2$O$_3$ (black) and Pt-Sn/γ-Al$_2$O$_3$ (red) catalysts after the (a) 1st and (b) 10th PDH cycles.
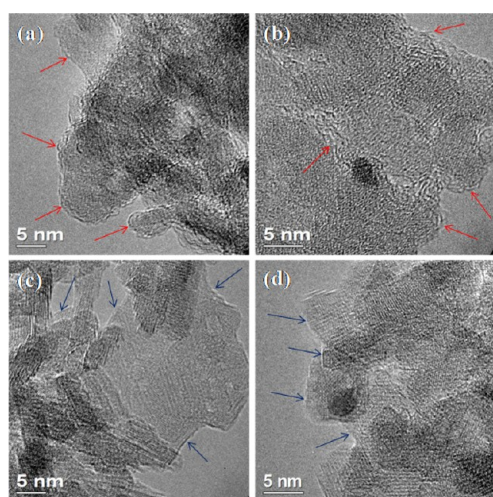
Figure 3. HRTEM images of the spent 10-PDH cycle Pt-Sn/γ-Al$_2$O$_3$ catalyst before (a and b) and after oxidative regeneration (c and d). The red arrows in panels a and b indicate the presence of carbon deposits on the surface of alumina, whereas the blue arrows in panels c and d indicate the removal of carbon from the surface of alumina after oxidative regeneration.

HAADF-STEM images of Pt/γ-Al$_2$O$_3$ before and after PDH, and their corresponding particle size distributions, are shown in Figure 4. The catalyst initially contains highly dispersed, very
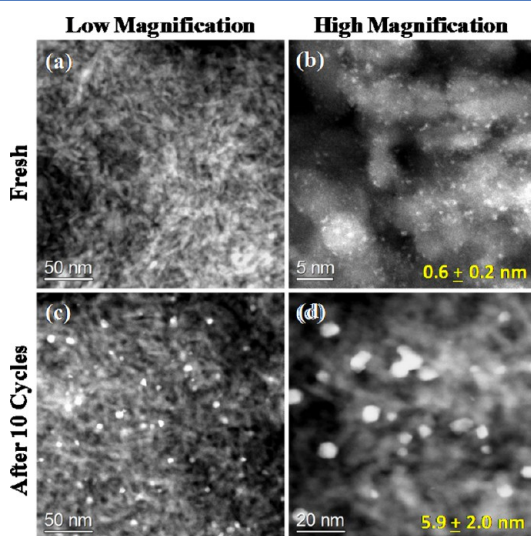
Figure 4. HAADF-STEM images at low (left) and high (right) magnifications of Pt/γ-Al$_2$O$_3$ as prepared (a and b) and after 10 PDH cycles (c and d). The mean diameter is indicated on the image with particle size distributions shown in the Supporting Information (Figure S2).

small metallic Pt nanoparticles [$\bar{d} = 0.6 \pm 0.2$ nm (Figure 4b)] in the absence of large Pt nanoparticles observed at lower magnifications (Figure 4a). After 10 PDH cycles, Pt has sintered into larger nanoparticles [$\bar{d} = 5.9 \pm 2.0$ nm (Figure 4c,d)] with very few of the smaller <1 nm Pt particles remaining after reaction. The complete particle size distribution (PSD) is shown in Figure S2.

In the Pt-Sn/γ-Al$_2$O$_3$ catalyst (Figure 5), we also see highly dispersed, very small metallic nanoparticles in the fresh catalyst [$\bar{d} = 0.8 \pm 0.2$ nm (Figure 5b)] in the absence of large Pt-Sn
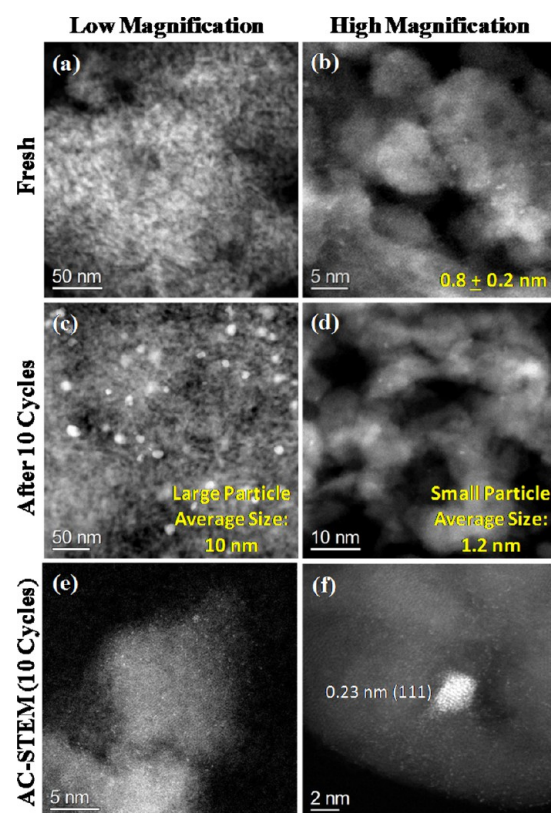

Figure 5. HAADF-STEM images at low (left) and high (right) magnifications of Pt-Sn/γ-Al$_2$O$_3$ as prepared (a and b) and after 10 PDH cycles (c and d). The mean diameter is indicated in image b, and two means when the size distribution is bimodal (c and d) (see Figure S3 for the complete particle size distribution). AC-STEM images after 10 PDH cycles (e and f), showing isolated Sn atoms as well as small metallic clusters. The measured d spacing in panel f is indexed to Pt$_3$Sn.

particles (Figure 5a). After three PDH cycles, some of the Pt-Sn particles have sintered (Figure S3a) while the majority have remained small and dispersed after reaction [$\bar{d} = 1.2 \pm 0.3$ nm (Figure S3b)]. After 10 PDH cycles, Pt-Sn/γ-Al$_2$O$_3$ reveals a bimodal distribution that is best shown in images at different magnifications; Figure 5c shows the large particle average to be $\bar{d} = 10$ nm, while Figure 5d shows the small particle average to be $\bar{d} = 1.2$ nm. The complete size distribution is shown in Figure S3c. The aberration-corrected (AC)-STEM images also show isolated single-atom species on this spent catalyst (Figure 5e) and small clusters of the Pt$_3$Sn phase (Figure 5f). EDS analysis (Figure 6) suggests that the atomically dispersed species are composed of Sn, because we can detect Sn in this sample even in regions devoid of any metallic nanoparticles. These atomically dispersed species represent Sn atoms strongly bound to the alumina support that are stable even after extended reactions at elevated temperatures.

The Pt-Sn/γ-Al$_2$O$_3$ spent catalyst after the 10th cycle was subjected to one additional oxidative treatment at 600 °C in flowing O$_2$/He for 1 h, followed by H$_2$ reduction for 45 min, to study regeneration of the catalyst. The particle size distribution remained bimodal (Figure S4), with larger particles such as those shown in panels a and b of Figure 7, and highly dispersed species shown in panels c and d of Figure 7. The larger particles shown in panels a and b show lattice fringes having d spacings of 0.14 and 0.23 nm, which can be indexed to the Pt$_3$Sn (220)
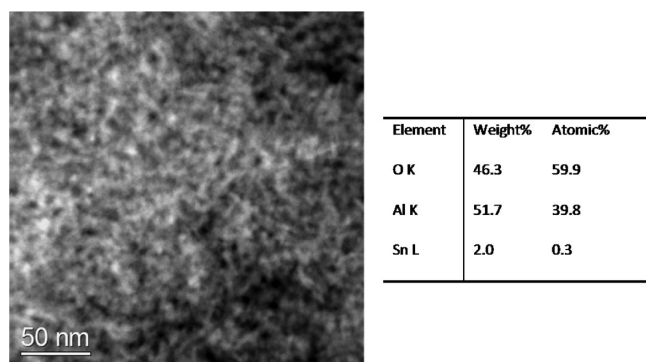
Element	Weight%	Atomic%
O K	46.3	59.9
Al K	51.7	39.8
Sn L	2.0	0.3

Figure 6. EDS analysis showing the average composition of the Pt-Sn/γ-Al$_2$O$_3$ catalyst after 10 PDH cycles. Only Sn is present on the alumina support in regions where there are no obvious metallic particles.

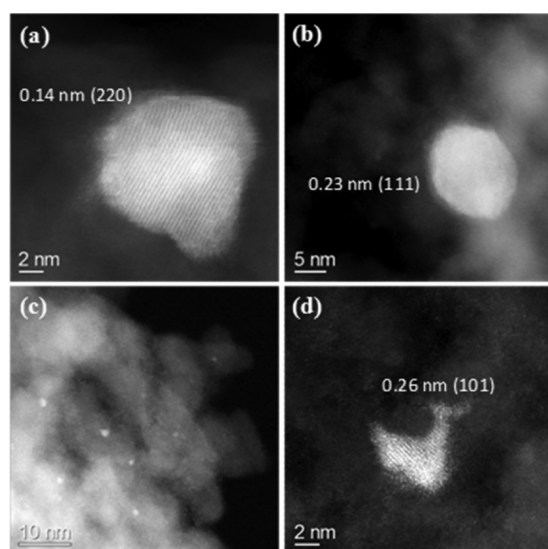**Figure 7.** AC-STEM images of the Pt-Sn/γ-Al$_2$O$_3$ catalyst after the 10th PDH cycle subjected to an oxidative regeneration treatment. The >10 nm particles in this oxidatively treated catalyst can be indexed to the Pt$_3$Sn phase and are difficult to redisperse (a and b) under our conditions (600 °C in O$_2$/He). On the other hand, smaller Pt-Sn particles are easier to subject to attrition (see Figure 10), leaving behind atomically dispersed species and subnanometer-sized clusters (c and d). Irregularly shaped SnO$_2$ particles (d) remain because the Pt has migrated away [d spacing indexed to SnO$_2$ (101)].

Figure 8. Pt and Sn atomic compositions of individual subnanometer clusters in the fresh Pt-Sn/γ-Al$_2$O$_3$ catalyst, as measured by EDS analysis.

Figure 9. Pt and Sn atomic compositions of individual subnanometer clusters in the regenerated Pt-Sn/γ-Al$_2$O$_3$ catalyst, as measured by EDS analysis. Some clusters containing pure Pt were detected due to Pt redispersion.

and (111) lattice planes, respectively. These particles are larger than 10 nm in size and have apparently remained intact without undergoing any change during the oxidative regeneration step. Figure 7c shows an image of another region of this same catalyst showing the existence of subnanometer Pt clusters. The size of the clusters is very similar to those seen in the fresh catalyst. EDS analysis (Figures 8 and 9) allows determination of Pt and Sn compositions in these subnanometer clusters for the fresh and regenerated Pt-Sn/γ-Al$_2$O$_3$ catalysts. There are some clusters in the regenerated catalyst that are 100% Pt; however, the majority of these particles are subnanometer Pt-Sn bimetallic clusters. While it is possible for EDS analysis to pick up X-rays from the surrounding support (which contains atomically dispersed Sn), we rule this out because we are able to find regions devoid of Sn. This indicates that the tightly collimated beam in the STEM provides EDS analysis
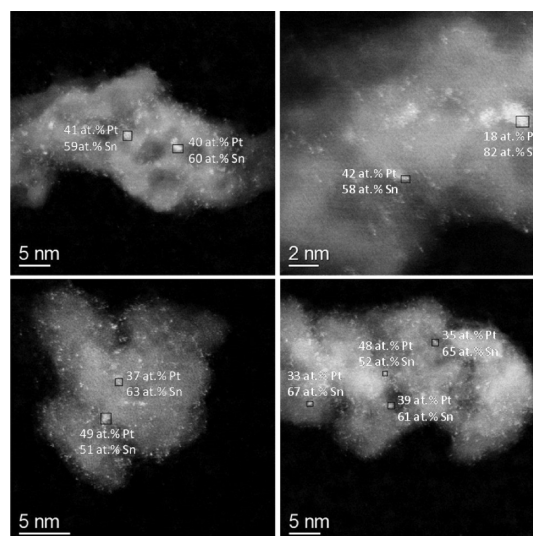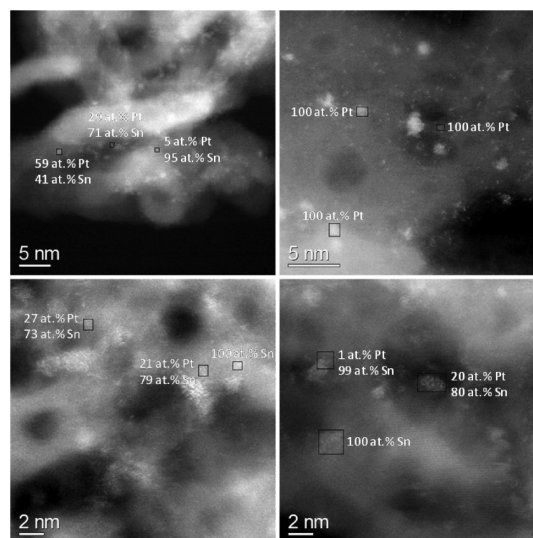
exclusively from regions where the beam is focused (as shown in the boxes in Figure 9).

4. DISCUSSION

It is well-known from the continuous catalyst regeneration (CCR) step in the UOP Oleflex dehydrogenation process that coke combustion and Pt redispersion occur via treatment of the catalyst in a chlorine/air mixture.[1,46] In this work, our catalysts are treated with O$_2$ and in the absence of a halide. From the AC-STEM images and bimodal particle size distribution shown in Figure 7 and Figure S4, respectively, it appears that >10 nm Pt$_3$Sn particles cannot be easily redispersed because treatment under oxidizing conditions is not aggressive enough for complete Pt redispersion in the absence of a halide. Nonetheless, we redisperse a portion of the Pt-Sn particles to subnanometer Pt species during the oxidative regeneration step,

and the presence of the redispersed subnanometer Pt species helps explain the regeneration in catalyst activity that is seen after each cycle in Figure 1. The image in Figure 7d also shows isolated single atoms, which were seen also in the initial Pt-Sn/γ-Al$_2$O$_3$ catalyst material in panels e and f of Figure 5. These single atoms represent oxidized Sn strongly bound to the alumina support, which survive multiple cycles of PDH followed by oxidative regeneration. Additional HAADF-STEM images are presented in Figure 10 showing various
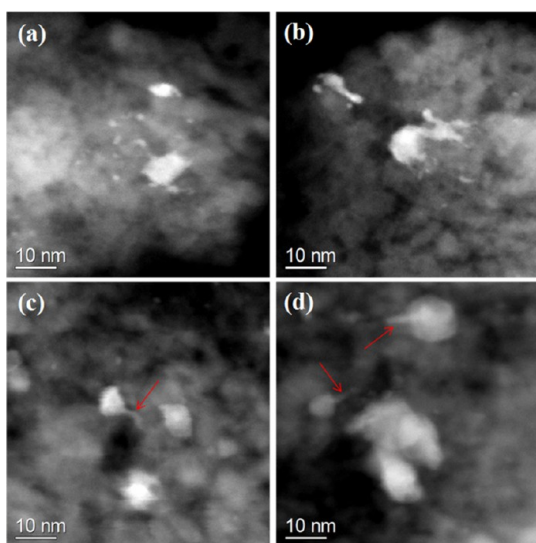

Figure 10. HAADF-STEM images of the spent Pt-Sn/γ-Al$_2$O$_3$ catalyst after oxidative regeneration, which show attrition of larger Pt-Sn particles into smaller particles (a and b) and particles with "tails" (c and d), as shown by red arrows. These "tails" represent wetting of the alumina support by SnO$_2$.

stages of the oxidative regeneration process. We see attrition of the smaller Pt-Sn nanoparticles, which leave behind SnO$_2$ in the form of irregular shaped particles or "tails". These "tails" represent wetting of the alumina support by SnO$_2$. Such particles were not seen in the monometallic Pt catalyst after the same oxidative regeneration step (Figure S5). Therefore, we postulate that the process of oxidative redispersion does not occur on the monometallic Pt/γ-Al$_2$O$_3$ catalyst. This is because atomically dispersed Sn oxide is not present on the monometallic catalyst. These atomically dispersed Sn species help provide nucleation sites to form subnanometer Pt clusters during oxidative regeneration. During the initial catalyst preparation, the highly hydroxylated γ-Al$_2$O$_3$ appears to provide plenty of nucleation sites, but subsequent high-temperature reaction and regeneration steps lead to a loss of these nucleation sites on the alumina support. For this reason, the monometallic Pt/γ-Al$_2$O$_3$ catalyst does not undergo regeneration (Figure 11a,b). In the bimetallic Pt-Sn/γ-Al$_2$O$_3$ catalyst, Sn remains anchored to the alumina, providing the atomically dispersed sites needed for the regeneration of the catalyst, leading to facile Pt redispersion (Figure 11c,d).

The tell-tale signs of oxidative regeneration, attrition of large Pt-Sn particles or the presence of particles with "tails", are absent on the monometallic catalyst (Figure 10). We attribute this difference to a lack of suitable nucleation sites on the alumina support (Figure 11). Subnanometer Pt clusters in the fresh Pt/γ-Al$_2$O$_3$ catalyst are irreversibly lost after successive reaction and regeneration cycles (Figure 4), leading to
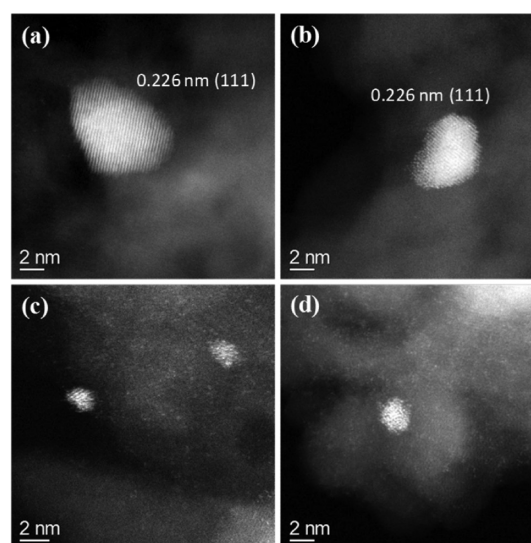

Figure 11. AC-STEM images of the Pt/γ-Al$_2$O$_3$ (a and b) and Pt-Sn/γ-Al$_2$O$_3$ (c and d) catalysts after 10 PDH cycles. No single atoms are present in Pt/γ-Al$_2$O$_3$, but isolated single atoms are abundant on the bimetallic catalyst. These single atoms are needed to regenerate the catalyst by redispersion of Pt, as in the case of Pt-Sn/γ-Al$_2$O$_3$.

significant loss of activity and propene selectivity over the 10 cycles in our study (Figure 1 and Table 1). In contrast, the bimetallic Pt-Sn/γ-Al$_2$O$_3$ catalyst continues to be regenerated after each cycle, with only minor losses of activity and selectivity. The AC-STEM images in Figures 5 and 7 therefore demonstrate an important role played by Sn in addition to its role as a promoter in enhancing propene selectivity and in suppressing coke formation. Atomically dispersed Sn is present on alumina even after multiple reaction cycles involving oxidative regeneration, providing the needed nucleation sites for Pt to be redispersed and re-creating subnanometer Pt−Sn clusters. The similarity in particle size distribution for Pt and Pt-Sn catalysts in the fresh catalyst material confirms the role of the highly dispersed species in this reaction. We therefore infer that the loss of activity of Pt-Sn/γ-Al$_2$O$_3$ is primarily due to the sintering of the alloyed Pt-Sn species, which are partially restored during oxidative regeneration. The presence of a bimodal particle size distribution suggests that some of the activity is lost due to the formation of larger metallic particles.

The temperature at which oxidative regeneration is performed may play an important role in the Pt redispersion and, hence, catalytic activity of Pt-Sn/γ-Al$_2$O$_3$. In a previous study of Pt-Ga/Al$_2$O$_3$ catalysts, we treated these catalysts at different temperatures, after which Pt dispersion was measured by CO chemisorption.[2] When the catalyst was treated in O$_2$ and He at 550 °C, we observed good Pt dispersion (∼25%), but when the catalyst was treated in O$_2$ and He at 650 °C, there was a significant decrease in the level of Pt dispersion (∼10%). We suspect there may be a similar trend in which there is a critical oxidative regeneration temperature between 550 and 650 °C for Pt to redisperse as subnanometer species in the Pt-Sn/γ-Al$_2$O$_3$ catalyst. In this work, the oxidative regeneration temperature of 600 °C may be critical for the regeneration of Pt-Sn and other bimetallic catalysts for PDH.

A previous high-energy resolution X-ray absorption study (HERFD XANES) of Pt/γ-Al$_2$O$_3$ and Pt-Sn/γ-Al$_2$O$_3$ supports this model of catalyst regeneration.[19] During oxidative regeneration, the Sn in the sintered Pt-Sn alloy was oxidized

and likely segregated from the alloy as SnO_2 particles. Pt dispersion was restored after subsequent H_2 reduction, leading to formation of new Pt-Sn alloy clusters. While HERFD XANES provides averaged information, the spatially resolved information via AC-STEM in this study helps in the assembly of a more complete picture of the oxidative regeneration process of Pt/γ-Al$_2$O$_3$ catalysts.

Because of the high current density in the AC-STEM probe, atoms could be ejected from a metallic nanoparticle and redeposit in the vicinity on the support. However, the electron beam current used in this study did not cause such artifacts; otherwise, we would have observed Pt atoms in the Pt/γ-Al$_2$O$_3$ catalyst. Panels a and b of Figure 11 clearly show that no dispersed Pt atoms are present in the Pt/γ-Al$_2$O$_3$ sample in the vicinity of the nanoparticles. The isolated atoms that are seen in the spent Pt-Sn/γ-Al$_2$O$_3$ sample (Figure 11c,d) are Sn atoms bound strongly to the alumina support, and they are also present in the fresh Pt-Sn/γ-Al$_2$O$_3$ sample (Figure S6). Once again, Sn is detected by EDS (Figure 6) and via AC-STEM (Figure S6) in regions without any obvious metallic particles; hence, it cannot be due to an electron beam artifact. The presence of such dispersed Sn was also implied in previous work using HERFD-XANES spectroscopy; AC-STEM provides direct visual confirmation of the presence of dispersed Sn in this sample.

5. CONCLUSIONS

The addition of Sn to Pt/γ-Al$_2$O$_3$ increases propene selectivity, and Sn provides the necessary nucleation sites to redisperse Pt atoms and to re-create, at least partially, subnanometer Pt clusters in the spent catalyst after oxidative regeneration. The critical difference between the monometallic Pt/γ-Al$_2$O$_3$ and the bimetallic Pt-Sn/γ-Al$_2$O$_3$ catalysts lies in the ability to re-form the catalytically active highly dispersed Pt species. This study shows that while coke formation occurs on both catalysts, the amount of coke does not correlate with the observed (loss in) reactivity. We further see that larger ($\sim$10 nm) Pt$_3$Sn particles in spent Pt-Sn/γ-Al$_2$O$_3$ show low propane dehydrogenation activity in this reaction. The presence of stable, atomically dispersed Sn species is an important finding and could lead to the better design of regenerable catalysts for a wide variety of applications. Other promoters, such as Ga, may play a similar role[2] and will be the subject of future study.

ASSOCIATED CONTENT

Ⓢ Supporting Information

The Supporting Information is available free of charge on the ACS Publications website at DOI: 10.1021/acscatal.5b02917.

> Operando Raman spectra of Pt/γ-Al$_2$O$_3$ and Pt-Sn/γ-Al$_2$O$_3$ after the 1st, 3rd, and 10th PDH cycles; Pt particle size distribution of Pt/γ-Al$_2$O$_3$ before PDH and after 10 PDH cycles; HAADF-STEM images of Pt-Sn/γ-Al$_2$O$_3$ after three PDH cycles; Pt-Sn particle size distribution before PDH and after the 3rd and 10th PDH cycles; particle size distributions of Pt/γ-Al$_2$O$_3$ and Pt-Sn/γ-Al$_2$O$_3$ after 10 PDH cycles and after oxidative regeneration; HAADF-STEM images of Pt/γ-Al$_2$O$_3$ after oxidative regeneration; and AC-STEM images of Pt-Sn/γ-Al$_2$O$_3$ before PDH and after 10 PDH cycles (PDF)

AUTHOR INFORMATION

Corresponding Authors
*E-mail: datye@unm.edu.
*E-mail: b.m.weckhuysen@uu.nl.

Author Contributions
H.N.P. and J.J.H.B.S. contributed equally to this work.

Notes
The authors declare no competing financial interest.

REFERENCES

(1) (a) Bricker, J. C. *Top. Catal.* **2012**, *55*, 1309−1314. (b) Sattler, J. H. H. B.; Ruiz-Martinez, J.; Santillan-Jimenez, E.; Weckhuysen, B. M. *Chem. Rev.* **2014**, *114*, 10613−10653.

(2) Sattler, J. J. H. B.; Gonzalez-Jimenez, I. D.; Luo, L.; Stears, B. A.; Malek, A.; Barton, D. G.; Kilos, B. A.; Kaminsky, M. P.; Verhoeven, T.; Koers, E. J.; Baldus, M.; Weckhuysen, B. M. *Angew. Chem., Int. Ed.* **2014**, *53*, 9251−9256.

(3) Nykanen, L.; Honkala, K. *ACS Catal.* **2013**, *3*, 3026−3030.

(4) Liu, X.; Zhou, Y. M.; Zhang, Y. W.; Duan, Y. Z.; Xue, M. W.; Wan, L. H. *China Pet. Process. Petrochem. T.* **2011**, *13*, 45−52.

(5) Won, W.; Lee, K. S.; Lee, S.; Jung, C. *Comput. Chem. Eng.* **2010**, *34*, 508−517.

(6) Coperet, C. *Chem. Rev.* **2010**, *110*, 656−680.

(7) Chen, M.; Xu, J.; Su, F. Z.; Liu, Y. M.; Cao, Y.; He, H. Y.; Fan, K. N. *J. Catal.* **2008**, *256*, 293−300.

(8) Zheng, B.; Hua, W. M.; Yue, Y. H.; Gao, Z. *J. Catal.* **2005**, *232*, 143−151.

(9) Li, R. X.; Wong, N. B.; Tin, K. C.; Chen, J. R.; Li, X. J. *Catal. Lett.* **1998**, *50*, 219−223.

(10) Padro, C. L.; de Miguel, S. R.; Castro, A. A.; Scelza, O. A. In *Catalyst Deactivation 1997*; Bartholomew, C. H., Fuentes, G. A., Eds.; Elsevier: Amsterdam, 1997; Vol. *111*, pp 191−198.

(11) McFarland, E. *Science* **2012**, *338*, 340−342.

(12) Chowdhury, A. D.; Weding, N.; Julis, J.; Franke, R.; Jackstell, R.; Beller, M. *Angew. Chem., Int. Ed.* **2014**, *53*, 6477−6481.

(13) Nijhuis, T. A.; Tinnemans, S. J.; Visser, T.; Weckhuysen, B. M. *Phys. Chem. Chem. Phys.* **2003**, *5*, 4361−4365.

(14) Bhasin, M. M.; McCain, J. H.; Vora, B. V.; Imai, T.; Pujado, P. R. *Appl. Catal., A* **2001**, *221*, 397−419.

(15) Weckhuysen, B. M.; Schoonheydt, R. A. *Catal. Today* **1999**, *51*, 223−232.

(16) Kwak, J. H.; Hu, J. Z.; Mei, D.; Yi, C. W.; Kim, D. H.; Peden, C. H. F.; Allard, L. F.; Szanyi, J. *Science* **2009**, *325*, 1670−1673.

(17) Mei, D. H.; Kwak, J. H.; Hu, J. Z.; Cho, S. J.; Szanyi, J.; Allard, L. F.; Peden, C. H. F. *J. Phys. Chem. Lett.* **2010**, *1*, 2688−2691.

(18) Vu, B. K.; Song, M. B.; Ahn, I. Y.; Suh, Y. W.; Suh, D. J.; Kim, W. I.; Koh, H. L.; Choi, Y. G.; Shin, E. W. *Appl. Catal., A* **2011**, *400*, 25−33.

(19) Iglesias-Juez, A.; Beale, A. M.; Maaijen, K.; Weng, T. C.; Glatzel, P.; Weckhuysen, B. M. *J. Catal.* **2010**, *276*, 268−279.

(20) de Miguel, S. R.; Jablonski, E. L.; Castro, A. A.; Scelza, O. A. *J. Chem. Technol. Biotechnol.* **2000**, *75*, 596−600.

(21) Lin, L. W.; Yang, W. S.; Jia, J. F.; Xu, Z. S.; Zhang, T.; Fan, Y. N.; Kou, Y.; Shen, J. Y. *Sci. China, Ser. B: Chem.* **1999**, *42*, 571−580.

(22) Mongkhonsi, T.; Prasertdham, P.; Saengpoo, A.; Pinitniyom, N.; Jaikaew, B. *Korean J. Chem. Eng.* **1998**, *15*, 486−490.

(23) Jia, J. F.; Lin, L. W.; Shen, J. Y.; Xu, Z. S.; Zhang, T.; Liang, D. B.; Chen, Y. *Sci. China, Ser. B: Chem.* **1998**, *41*, 606−615.

(24) Praserthdam, P.; Mongkhonsi, T.; Kunatippapong, S.; Jaikaew, B.; Lim, N. In *Catalyst Deactivation 1997*; Bartholomew, C. H., Fuentes, G. A., Eds.; Elsevier: Amsterdam, 1997; Vol. *111*, pp 153−158.

(25) Sun, P. P.; Siddiqi, G.; Chi, M. F.; Bell, A. T. *J. Catal.* **2010**, *274*, 192−199.

(26) Siddiqi, G.; Sun, P. P.; Galvita, V.; Bell, A. T. *J. Catal.* **2010**, *274*, 200−206.

(27) Lapidus, A. L.; Pavlova, V. A.; Nekrasov, N. V.; Dergachev, A. A. *Pet. Chem.* **2010**, *50*, 114−119.

(28) Jablonski, E. L.; Castro, A. A.; Scelza, O. A.; de Miguel, S. R. *Appl. Catal., A* **1999**, *183*, 189−198.

(29) Han, Z. P.; Li, S. R.; Jiang, F.; Wang, T.; Ma, X. B.; Gong, J. L. *Nanoscale* **2014**, *6*, 10000−10008.

(30) Sokolov, S.; Stoyanova, M.; Rodemerck, U.; Linke, D.; Kondratenko, E. V. *J. Catal.* **2012**, *293*, 67−75.

(31) Resini, C.; Lucarelli, C.; Taillades-Jacquin, M.; Liew, K. E.; Gabellini, I.; Albonetti, S.; Wails, D.; Roziere, J.; Vaccari, A.; Jones, D. *Int. J. Hydrogen Energy* **2011**, *36*, 5972−5982.

(32) Lucarelli, C.; Albonetti, S.; Vaccari, A.; Resini, C.; Taillades, G.; Roziere, J.; Liew, K. E.; Ohnesorge, A.; Wolff, C.; Gabellini, I.; Wails, D. *Catal. Today* **2011**, *175*, 504−508.

(33) Reyes-Carmona, A.; Gianotti, E.; Taillades-Jacquin, M.; Taillades, G.; Roziere, J.; Rodriguez-Castellon, E.; Jones, D. *J. Catal. Today* **2013**, *210*, 26−32.

(34) Taillades-Jacquin, M.; Resini, C.; Liew, K. E.; Taillades, G.; Gabellini, I.; Wails, D.; Roziere, J.; Jones, D. *Appl. Catal., B* **2013**, *142−143*, 112−118.

(35) Pearson, K.; Kafer, T.; Kraaij, G.; Worner, A. *Int. J. Hydrogen Energy* **2015**, *40*, 1367−1378.

(36) Watwe, R. M.; Cortright, R. D.; Mavrikakis, M.; Norskov, J. K.; Dumesic, J. A. *J. Chem. Phys.* **2001**, *114*, 4663−4668.

(37) Wu, J.; Mallikarjun Sharada, S.; Ho, C.; Hauser, A. W.; Head-Gordon, M.; Bell, A. T. *Appl. Catal., A* **2015**, *506*, 25−32.

(38) Hauser, A. W.; Gomes, J.; Bajdich, M.; Head-Gordon, M.; Bell, A. T. *Phys. Chem. Chem. Phys.* **2013**, *15*, 20727−20734.

(39) Wu, J.; Peng, Z. M.; Bell, A. T. *J. Catal.* **2014**, *311*, 161−168.

(40) Vu, B. K.; Shin, E. W. *Catal. Lett.* **2011**, *141*, 699−704.

(41) Shi, L.; Deng, G.-M.; Li, W.-C.; Miao, S.; Wang, Q.-N.; Zhang, W.-P.; Lu, A.-H. *Angew. Chem., Int. Ed.* **2015**, *54*, 13994−13998.

(42) Vu, B. K.; Song, M. B.; Ahn, I. Y.; Suh, Y. W.; Suh, D. J.; Kim, J. S.; Shin, E. W. *J. Ind. Eng. Chem.* **2011**, *17*, 71−76.

(43) Sattler, J.; Beale, A. M.; Weckhuysen, B. M. *Phys. Chem. Chem. Phys.* **2013**, *15*, 12095−12103.

(44) Moodley, D. J.; van Schalkwyk, C.; Spamer, A.; Botha, J. M.; Datye, A. K. *Appl. Catal., A* **2007**, *318*, 155−159.

(45) Pham, H. N.; Anderson, A. E.; Johnson, R. L.; Schwartz, T. J.; O'Neill, B. J.; Duan, P.; Schmidt-Rohr, K.; Dumesic, J. A.; Datye, A. K. *ACS Catal.* **2015**, *5*, 4546−4555.

(46) UOP Oleflex Process for Light Olefin Production; http://pet-oil.blogspot.nl/2012/10/uop-oleflex-process-for-light-olefin.html (accessed October 23, 2013).